Active Aerodynamic Load Reduction on a Rotorcraft Fuselage with Rotor Effects - A CFD Validation Effort

Brian G. Allan
Research Scientist

Norman W. Schaeffler
Research Scientist

Luther N. Jenkins
Senior Research Scientist

Chung-Sheng Yao
Senior Research Scientist

Flow Physics and Control Branch
NASA Langley Research Center
Hampton, Virginia, USA

Oliver D. Wong
Senior Research Scientist

Philip E. Tanner
Research Scientist

United States Army Research, Development, and Engineering Command
Aviation Development Directorate / AFDD (AMRDEC)
Hampton, Virginia, USA

ABSTRACT

A rotorcraft fuselage is typically designed with an emphasis on operational functionality with aerodynamic efficiency being of secondary importance. This results in a significant amount of drag during high-speed forward flight that can be a limiting factor for future high-speed rotorcraft designs. To enable higher speed flight, while maintaining a functional fuselage design (i.e., a large rear cargo ramp door), the NASA Rotary Wing Project has conducted both experimental and computational investigations to assess active flow control as an enabling technology for fuselage drag reduction. This paper will evaluate numerical simulations of a flow control system on a generic rotorcraft fuselage with a rotor in forward flight using OVERFLOW, a structured mesh Reynolds-averaged Navier-Stokes flow solver developed at NASA. The results are compared to fuselage forces, surface pressures, and PIV flow field data obtained in a wind tunnel experiment conducted at the NASA Langley 14-by 22-Foot Subsonic Tunnel where significant drag and download reductions were demonstrated using flow control. This comparison showed that the Reynolds-averaged Navier-Stokes flow solver was unable to predict the fuselage forces and pressure measurements on the ramp for the baseline and flow control cases. While the CFD was able to capture the flow features, it was unable to accurately predict the performance of the flow control.

NOTATION

A_{CS}	=	fuselage body cross-sectional area (maximum), in^2
a_∞	=	freestream speed of sound, ft/s
A_p	=	upper pylon cutout area, in^2
A_t	=	tail cross-sectional area, in^2
C_D	=	fuselage drag coefficient, $D/(q_\infty A_{CS})$
C_L	=	fuselage lift coefficient, $L/(q_\infty A_{CS})$
C_p	=	pressure coefficient, $(p-p_s)/q_\infty$
C_T	=	rotor thrust coefficient, $T/\rho_\infty \pi R^2 (\Omega R)^2$
C_T/σ	=	blade loading coefficient
C_μ	=	momentum coefficient,$\equiv \sum(\rho_j A_j U_j^2)/(q_\infty A_{CS})$
p	=	pressure, psi
p_s	=	static pressure, psi
q_∞	=	freestream dynamic pressure, $\frac{1}{2}\rho_\infty U_\infty^2$, psi
R	=	rotor radius, inches
R_F	=	reference rotor radius, inches
Re	=	Reynolds number, $U_\infty(2R_F)/\nu$
T_t	=	total temperature, $^\circ R$
U	=	streamwise velocity component
U_∞	=	freestream velocity, ft/s
U_{tip}	=	rotor tip hover velocity, ft/s
U_j	=	jet exit velocity, ft/s
V	=	crossflow velocity component
VR	=	jet velocity ratio, U_j/U_∞
W	=	vertical velocity component
α_{fuse}	=	fuselage angle of attack, degrees
α_j	=	jet inclination angle, degrees
α_s	=	rotor shaft angle, degrees
μ	=	rotor advance ratio, $U_\infty \cos\alpha/(\Omega R)$
ν	=	kinematic viscosity, ft^2/s
ψ	=	rotor azimuth angle, degrees

Presented at the AHS 71st Annual Forum, Virginia Beach, Virginia, May 5–7, 2015. This material is declared a work of the U.S. Government and is not subject to copyright protection in the U.S. AMRDEC Public Release Control Number PR1614.

ρ = density, $slugs/ft^3$
σ = thrust weighted rotor solidity

Acronyms

AFC = Active Flow Control
AoA = Angle of Attack, degrees
CFD = Computational Fluid Dynamics
RANS = Reynolds-averaged Navier-Stokes
ROBIN = ROtor Body INteraction
VR = Velocity Ratio

Subscripts

j = jet
∞ = freestream

INTRODUCTION

The design of a rotorcraft fuselage places greater emphasis on function than aerodynamic efficiency. For example, the aft-facing ramp on certain rotorcraft fuselages used for transporting equipment is designed to load and unload cargo easily but contributes to significant drag at cruise due to the massive flow separation on the rear of the fuselage. The cruise drag of a rotary-wing aircraft is typically an order of magnitude higher than the cruise drag of a fixed-wing aircraft of the same gross weight (Ref. 1) and at high advance ratios, half the power supplied to the main rotor is used to overcome the aerodynamic forces on the fuselage (Ref. 2). Reducing the size and unsteadiness of the separated flow on the fuselage aft end can reduce the pressure drag contribution to the total drag and also help mitigate unsteady aerodynamic loads on the tail boom, stabilizers, and tail rotor.

Research on using flow control to reduce the size and unsteadiness of the separated region began in earnest in 2004-2005 when Martin, et al. (Ref. 3) and Ben-Hamou et al. (Ref. 4) demonstrated experimentally that the application of active flow control to achieve a reduction in fuselage drag is possible for an isolated fuselage (i.e., no rotor effects). In 2006, the NASA Rotary Wing (RW) Project initiated an integrated experimental and Computation Fluid Dynamics (CFD) research effort to investigate different approaches to achieve rotorcraft fuselage drag reduction using flow control (Ref. 5). As part of this research, NASA and the U.S. Army designed a non-proprietary fuselage based on an analytically defined geometry similar to the ROBIN (ROtor Body INteraction) fuselage (Ref. 6) developed in the late 1970s. A joint collaboration between NASA, the U.S. Army, and ONERA has resulted in the identification of a flow control strategy using CFD tools, predicting a 26% reduction in fuselage drag (Ref. 5). This flow control approach was then evaluated in a rotor environment using CFD, providing pre-test guidance to a 1/3 scale wind tunnel experiment conducted at the NASA Langley 14-by 22-Foot Subsonic Tunnel (Ref. 7). The wind tunnel experiments at the 14-by 22-Foot Subsonic Tunnel tested three different flow control approaches: sweeping jets, zero-net-mass-flux oscillatory blowing, and steady blowing (Refs. 8, 9).

A similar research effort was also initiated by ONERA within the Clean Sky project at about the same time as the NASA effort. The ONERA researchers used an open generic fuselage geometry designed at ONERA in the mid 1980s and developed a flow control strategy to reduce fuselage drag using CFD (Ref. 10). The flow control design was then successfully tested at the ONERA L1 wind tunnel, where they demonstrated a maximum fuselage drag reduction of 32% using steady blowing on an isolated fuselage (Ref. 11). This research further demonstrates that significant fuselage drag reduction is possible for rotorcraft at high-speed cruise; however, the effect of the rotor still needs to be addressed.

In this paper, we will compare and evaluate numerical simulation results to data from the rotor/fuselage wind tunnel test conducted at the NASA Langley 14-by 22-Foot Subsonic Tunnel (Ref. 9). The goals of this investigation were to evaluate the ability of a Reynolds-averaged Navier-Stokes (RANS) flow solver to predict the flow field for this configuration as well as the performance of the flow control system. Understanding the capabilities of CFD tools to model the performance of the flow control system will provide valuable insight into applying these tools to the designs of future drag reduction efforts.

NUMERICAL MODELING APPROACH

Flow Solver

The flow field for the fuselage was computed using the flow solver code OVERFLOW, developed at NASA (Refs. 12, 13). This code solves the compressible RANS equations using the diagonal scheme of Pulliam and Chaussee (Ref. 14) on structured grids using the overset grid framework of Steger, Dougherty, and Benek (Ref. 15). The RANS equations are solved implicitly using the Beam-Warming block tridiagonal scheme with a 4^{th} order central difference scheme for the inviscid flux terms. The Spalart Allmaras (SA) (Ref. 16) and Shear Stress Transport (SST) (Ref. 17) turbulence models were used for the numerical simulations with a Rotational/Curvature Correction (RCC) model, as implemented in OVERFLOW (Ref. 18). Time-accurate rotor/fuselage simulations used a dual-time stepping method with time steps equivalent to 0.125° rotor revolutions with 40 sub iterations per time step.

The blowing slots were simulated using a surface boundary condition, simplifying placement of the jets on the fuselage. The jet properties are defined by setting the mass flow ratio per unit area of $\rho_j U_j / \rho_\infty U_\infty$ and the total temperature ratio, $T_{tj}/T_{t\infty}$. For the slot boundary conditions, a jet blowing angle, α_j, is specified and is based on the local surface tangent, normal to the slot span. An α_j of 90° is therefore normal to the local surface and 0° is tangent. The simulations in this paper used a fixed $\alpha_j = 25°$ to match the experiment.

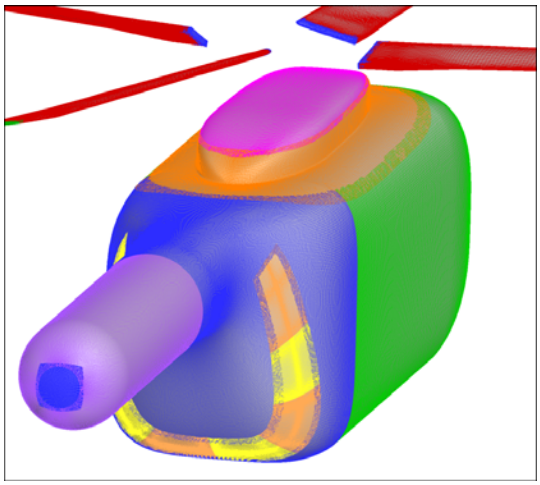

Fig. 1. Surface grids on the fuselage and rotor.

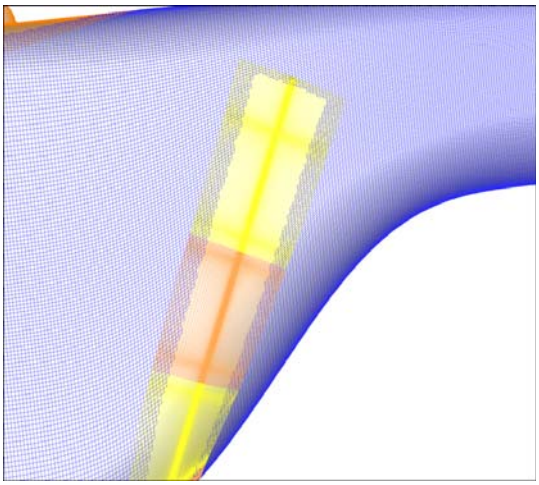

Fig. 2. Detail of grids used for flow control slots.

Grids

The grids, shown in Figs. 1 and 2, included five fuselage grids with eight refined overset grids to resolve the flow control jets on the surface and twelve grids for the four rotor blades. The rotor and body wakes were captured using grids with a uniform grid spacing equal to 10% of the rotor tip chord in all three directions. These wake grids extended 0.8 rotor radii downstream of the rotor tip path plane and 0.8 radii below the rotor hub center, capturing the rotor and fuselage wakes. Automatic background grids are generated by OVERFLOW and coarsened by doubling the cell size for each successive level of grids such that the far field boundary was approximately 52 rotor radii away from the hub center. The numerical simulations have a total of 200 million grid points with 71 million of these grid points used for the body and rotor volume grids.

Rotor Dynamics

The rotor dynamics were simulated using a loose coupling between the flow solver and the comprehensive rotorcraft code, CAMRAD-II (Refs. 19, 20). The rotor blades are modeled as nonelastic blades with flapping and lead/lag motions. In the rotor/fuselage simulations, a target rotor thrust is set and the comprehensive code adjusts the collective and cyclic inputs to match the commanded thrust while minimizing flapping. The blade motions from the comprehensive code are then used in the time-accurate CFD simulations. The aerodynamic forces on the rotor blades are then passed back to the comprehensive code and used to update the dynamic motion of the rotor blades and to trim the rotor, matching the target thrust while minimizing flapping. This loose coupling was performed every half revolution of the rotor.

EXPERIMENT

The wind tunnel experiments were conducted at the NASA Langley 14-by 22-Foot Subsonic Tunnel. This tunnel is a 770 foot closed circuit, single return, atomospheric wind tunnel (Ref. 21). The wind tunnel test was conducted in the closed test section configuration with the tunnel walls in place.

Wind Tunnel Model and Test Conditions

The modified ROBIN geometry, referred to as the ROBIN-mod7, was developed at NASA in collaboration with the U.S. Army as a representative generic helicopter fuselage with a large aft loading cargo section, typical of a commercial rotorcraft that encounters a large fuselage drag at high-speed. The fuselage geometry is analytically defined for ease of use in CFD validation efforts and as a standard generic fuselage geometry for evaluation of future flow control strategies (Ref. 5). As in the original ROBIN fuselage geometry, the fuselage scaling is based on a reference rotor radius, $R_F = 62.0$ inches with a total length of $2R_F$ (124 inches) as detailed in Figs. 3 and 4. Note that the rotor in this wind tunnel test had a radius of $R = 66.5$ inches as shown in Fig. 5 and is about 7% larger than the reference rotor radius, R_F. In order to mount the fuselage without disrupting the flow on the lower surface and ramp region, a portion of the tail section from $x/R_F = 1.694$ was removed to accommodate a sting support through the tail section.

Rotor Blades

The rotor blades were acquired specifically for a Pressure Sensitive Paint (PSP) validation test and were used in a hover test of Wong et al. (Ref. 22) at the 14-by 22-Foot Subsonic Tunnel Rotor Test Cell. The blade uses Government RC-series airfoils with the planform shown in Fig. 5. The rotor has a linear

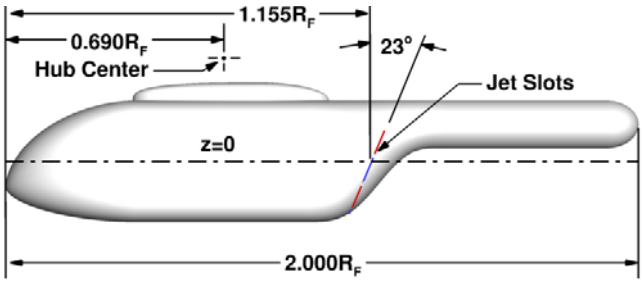

Fig. 3. Side view of the ROBIN-mod7 geometry with flow control blowing slots near the fuselage ramp region. Reference rotor radius $R_F = 62.0$ inches.

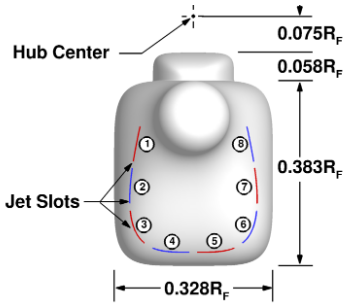

Fig. 4. Rear view of the ROBIN-mod7 geometry with flow control blowing slots near the fuselage ramp region. Reference rotor radius $R_F = 62.0$ inches and slot numbers labeled.

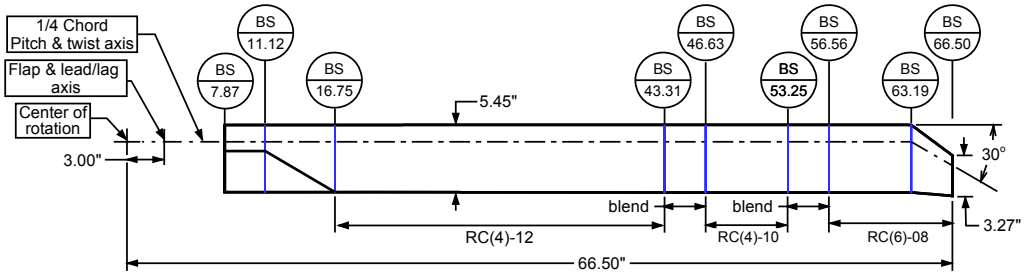

Fig. 5. Blade layout.

twist of -14° starting at Blade Station (BS) 16.75 and ending at the rotor tip. The blade has a chord length of 5.45 inches with a 30° tip sweep and a 3.27 inch tip chord length. Figure 5 shows a notch in the planform from BS 7.87 to 16.75. This notched out area contains a connector fairing to accommodate wiring from two pressure instrumented blades and is present on all four blades for symmetry. Figure 5 also shows the flap and lead/lag hinge to be collocated 3.00" from the hub center.

The rotor had a fixed rotational rate of 1150 RPM resulting in a hover tip Mach number of 0.6 and a shaft tilt angle of -2.5° relative to the fuselage. The free stream Mach number, for the cases investigated here, was 0.147 (100 knots), the rotor advance ratio was $\mu = 0.25$, and the thrust, given in terms of the blade loading coefficient of $C_T/\sigma = 0.075$. The fuselage was placed at an α_{fuse} of $-6°$, which is a typical attitude for a rotorcraft in cruise and a high drag configuration for the fuselage.

Fuselage Forces

Figure 6 shows the ROBIN-mod7 model in the 14-by 22-Foot Subsonic Tunnel test section with the tail section removed to accommodate the model support through the tail. The CFD simulations presented in this paper model the full fuselage without the model support geometry. To account for this difference, the CFD forces are computed up to fuselage station $x/R_F = 1.694$ where the wind tunnel model geometry ends. In the experiment, the fuselage and rotor forces were measured independently by two separate internal six-component strain gage force and moment balances. Therefore, the CFD did not need to model the hub since the forces on the hub are independent of the fuselage forces. However, rotor hub blockage and wake effects can have an impact on the fuselage forces but these effects are not explored in this paper.

Internal Model Pressure Corrections Since the wind tunnel fuselage model has an open tail and circular hole in the upper pylon, the internal model pressure forces will not cancel out as in a fully closed model. This results in a net internal pressure force, which is additive to the net force from the external flow. In the CFD force calculations, the internal pressure is defined as the freestream static pressure. Therefore, in order to compare the CFD and experiment forces, the experimental force data is corrected for forces resulting from a pressure difference between the free stream static and the internal pressure in the model. The following equations were used to correct both C_D and C_L for the open tail.

$$C_{D,corr,tail} = \frac{(p_i - p_\infty)A_t}{q_\infty A_{ref}} \cos(\alpha_{fuse}) \quad (1)$$

$$C_{L,corr,tail} = \frac{(p_i - p_\infty)A_t}{q_\infty A_{ref}} \sin(\alpha_{fuse}) \quad (2)$$

where p_i is the internal pressure of the model, A_t the tail cross sectional area, and A_{ref} the fuselage maximum cross sectional

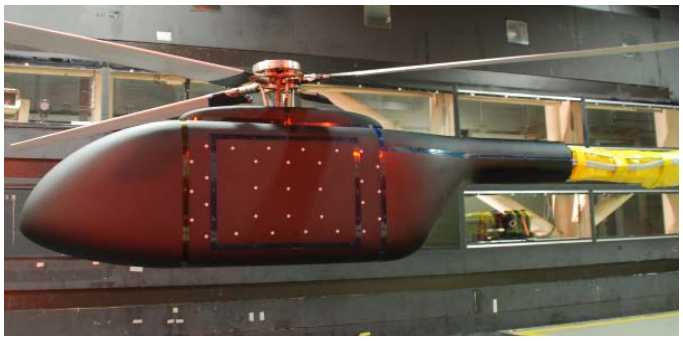

Fig. 6. ROBIN-mod7 model with rotor in 14-by 22-Foot Subsonic Tunnel

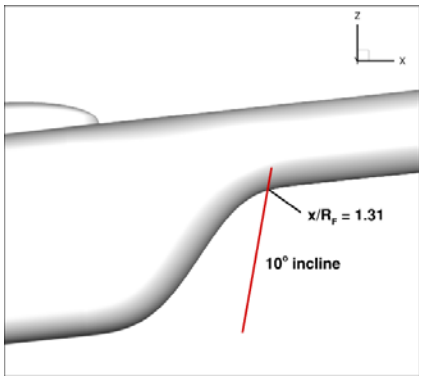

Fig. 7. Side view of ROBIN-mod7 fuselage ramp region at -6° AoA with location of PIV plane.

reference area.

Likewise, there is a 5 inch diameter circular cutout on the top of the fuselage pylon for the rotor shaft to pass through the fuselage. The drag and lift coefficient corrections for this circular cutout are made using the following equations,

$$C_{D,corr,pylon} = \frac{(p_i - p_\infty)A_p}{q_\infty A_{ref}} \sin(\alpha_{fuse}) \quad (3)$$

$$C_{L,corr,pylon} = \frac{(p_i - p_\infty)A_p}{q_\infty A_{ref}} \cos(\alpha_{fuse}) \quad (4)$$

where A_p is the area of the 5 inch circular hole on top of the upper pylon. The corrected drag and lift coefficients using the corrections for the open tail and open upper pylon are as follows.

$$C_{D,corr} = C_D + C_{D,corr,tail} + C_{D,corr,pylon} \quad (5)$$

$$C_{L,corr} = C_L + C_{L,corr,tail} + C_{L,corr,pylon} \quad (6)$$

Flow Control Approach

The flow control consists of a series of eight slots that form a nearly continuous U-shape on the aft region of the fuselage as depicted in Figs. 3 and 4. The U-shaped group of slots are aligned 23° from the vertical and located near the flow separation line. This configuration was found to work best in the isolated fuselage CFD study conducted by NASA and ONERA (Ref. 5). The slot height was set to 0.020 inches. The jet angle was $\alpha_j = 25^\circ$ to the local surface tangent, blowing downstream and normal to the local slot spanwise vector.

PIV Measurements

Stereo Particle Image Velocimetry (PIV) flow field measurements were made directly downstream of the fuselage ramp measuring the three components of the flow velocity. Figure 7 shows the location of the PIV plane relative to the fuselage at -6° AoA. The PIV plane was inclined 10° backwards relative to the tunnel vertical coordinate as depicted in Fig. 7. The PIV plane intersected the lower fuselage tail section at $x/R_F = 1.31$ in the body coordinate system. The flow field measurements used a Large Field-of-View PIV technique developed by Jenkins et al. (Ref. 23) and measured the three components of velocity in a 2.71 ft wide by 1.31 ft high plane. Over 200 images were sampled for a given rotor azimuthal angle providing a converged mean of the velocity vectors downstream of the ramp.

RESULTS

Time-accurate RANS simulations for the baseline and two steady blowing cases were performed using the SA and SST turbulence models. The CFD simulations are all performed at a fuselage AoA of -6°, rotor AoA of -8.5°, and a free-stream velocity of 100 knots with a rotor thrust, $C_T/\sigma = 0.075$, and rotor advance ratio, $\mu = 0.25$. The results from the CFD simulations are compared to the wind tunnel measured data.

Fuselage Forces

In this section, the mean fuselage drag and lift values from the CFD simulations will be compared to the measured forces from the internal balance in the experiment. The mean values from the CFD are computed from one complete rotor revolution after the forces reach a near periodic state. Figure 8 shows a time history of the fuselage drag and lift coefficients for the baseline case at $\alpha_{fuse} = -6^\circ$ with an advance ratio, $\mu = 0.25$, and a rotor thrust, $C_T/\sigma = 0.075$. From this figure, it can be seen that there are large oscillations in the fuselage drag and lift coefficients as a function of rotor azimuth. The large oscillations in the drag are a result of the pressure increase on the front of the fuselage imparted from the rotor as it passes over the nose section. Likewise, the lift oscillates from pressure fluctuations on the nose and tail sections. It is also noted

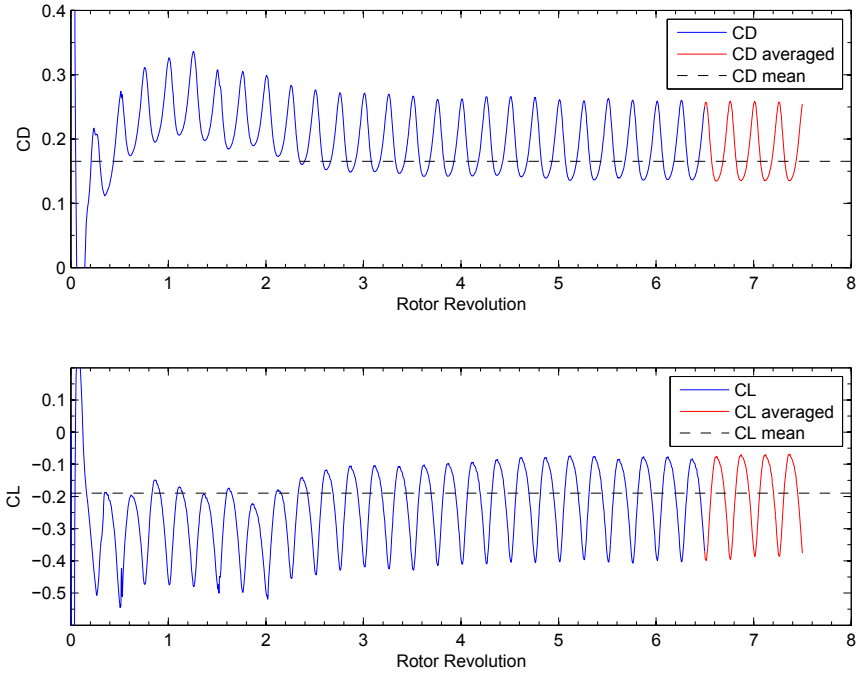

Fig. 8. Baseline ROBIN-mod7 fuselage drag and lift coefficient history for the SST turbulence model. Mean values (dashed line) calculated from last rotor revolution (red line); AoA $= -6^{\circ}$, $\mu = 0.25$, and $C_T/\sigma = 0.075$.

that the fuselage lift and drag coefficients reach a near periodic state after about 6 rotor revolutions, which is equivalent to approximately a flying distance of eight fuselage lengths.

Baseline Case The fuselage force comparisons of lift and drag for the baseline (no blowing) case are summarized in Table 1. The CFD results are broken down into viscous and pressure contributions. The experimental data shows both the measured fuselage forces along with the corrected forces. Applying the internal pressure corrections to the experimental C_D value results in a 0.021 reduction to a value of 0.225. The CFD results predict a C_D value of 0.198 for the SA turbulence model and 0.165 for the SST turbulence model. Both turbulence models under predict the baseline drag coefficient with the SA model results closer to the experiment. Table 1 also shows that the main difference between the two turbulence models is in the prediction of the pressure drag.

The corrected lift coefficient for the experiment is -0.287 where the internal pressure correction resulted in a 0.007 increase in the lift coefficient. This correction is small relative to the drag correction since the open area on the pylon is 3.5 times smaller than the open tail area. The SA turbulence model over predicts the download on the fuselage by 0.038 ($C_L = -0.325$) whereas the SST model under predicts the download by 0.097 ($C_L = -0.190$). Although the uncertainty of the measured lift coefficient on the fuselage is relatively high at ± 0.03, the predicted value for both models is outside the measure uncertainty.

AFC Steady Blowing Case: U-Configuration The drag and lift coefficients for steady blowing using the U-configuration (all 8 blowing slots) are given in Tables 2 and 3, respectively. This jet boundary condition was adjusted in order to match the experimental mass flow and resulted in a jet VR of 2.6. A jet momentum coefficient, C_μ, of 0.021 has also been computed using the following equation.

$$C_\mu = \frac{\dot{m}_j U_j}{q_\infty A_{CS}} \tag{7}$$

In addition to the viscous and pressure components, the CFD results in Tables 2 and 3 also provide the contribution of thrust from the jet mass flux. Table 2 shows that both the SA and SST turbulence models under predict the drag coefficient when compared to the experimental corrected value of $C_D = 0.166$. These differences are well outside the measurement accuracy of the experiment. It should be noted that the total C_D values in these tables include the viscous, pressure, and thrust forces since the thrust from the blowing was not subtracted from the experimental data. From the CFD simulations the thrust contribution for the drag coefficient is -0.020. Looking at Table 2 it can be seen that the major differences between the CFD results for the baseline and the AFC cases are the pressure and thrust components, with the viscous drag nearly the same. The pressure drag contribution between the two turbulence models is very different and is related to how well each model predicts the flow separation on the ramp.

Baseline Fuselage Force Summary
100 knots, $AoA = -6^\circ$, $\mu = 0.25$, and $C_T/\sigma = 0.075$

	$C_{D,visc}$	$C_{D,press}$	$C_{D,total}$		$C_{L,visc}$	$C_{L,press}$	$C_{L,total}$	
CFD SA	0.042	0.156	0.198		-0.002	-0.323	-0.325	
CFD SST	0.039	0.128	0.165		-0.002	-0.188	-0.190	
EXP			0.246	$\pm$ 0.009			-0.280	$\pm$ 0.03
EXP CORRECTED			0.225	$\pm$ 0.009			-0.287	$\pm$ 0.03

Table 1. Summary of fuselage drag and lift coefficients for the baseline (no AFC blowing) case.

AFC Fuselage Drag Summary
Jet VR = 2.6, U-configuration,100 knots, $AoA = -6^\circ$, $\mu = 0.25$, and $C_T/\sigma = 0.075$

	Jet VR	$\dot{m}(lbm/s)$	C_μ	$C_{D,visc}$	$C_{D,press}$	$C_{D,thrust}$	$C_{D,total}$	
CFD SA	2.6	0.164	0.021	0.044	0.088	-0.020	0.112	
CFD SST	2.6	0.164	0.021	0.041	0.113	-0.020	0.134	
EXP	2.6	0.164	0.021				0.184	$\pm$ 0.009
EXP CORRECTED	2.6	0.164	0.021				0.166	$\pm$ 0.009

Table 2. Summary of fuselage drag coefficient for AFC steady blowing for the U-configuration.

AFC Fuselage Lift Summary
Jet VR = 2.6, U-configuration, 100 knots, $AoA = -6^\circ$, $\mu = 0.25$, and $C_T/\sigma = 0.075$

	Jet VR	$\dot{m}(lbm/s)$	C_μ	$C_{L,visc}$	$C_{L,press}$	$C_{L,thrust}$	$C_{L,total}$	
CFD SA	2.6	0.164	0.021	-0.002	-0.172	0.002	-0.172	
CFD SST	2.6	0.164	0.021	-0.002	-0.140	0.002	-0.139	
EXP	2.6	0.164	0.021				-0.171	$\pm$ 0.03
EXP CORRRECTED	2.6	0.164	0.021				-0.178	$\pm$ 0.03

Table 3. Summary of fuselage lift coefficient for AFC steady blowing for the U-configuration.

In Table 3 The corrected lift coefficient for the experiment is -0.178 with the SA model closely predicting the experiment at -0.172 and the SST model under predicting C_L at -0.139. The SA model is within the uncertainty of the measured fuselage C_L, while the SST model under predicts the fuselage download by 0.039 ($C_L = -0.139$). The thrust contribution to lift is small since the slots are primarily aligned with the flow. For this case the thrust from the jets in the lift direction is $C_{L,thrust} = 0.002$.

AFC Steady Blowing Case: Ux45-Configuration Next the Ux45-configuration is simulated by turning off the bottom two slots (slot 4 and 5). The drag and lift coefficients for this case are shown in Tables 4 and 5, respectively. Experimentally, this configuration showed almost no change in the fuselage drag but did show a reduction in download force on the fuselage. The results in Table 4 show that the experimental drag is essentially the same for both the U to Ux45-configuration, while the SA and SST turbulence model simulations predict an increase in fuselage drag when compared to the U-configuration. Therefore, the CFD is unable to capture the correct trends in terms of the drag staying the same between these two slot configurations.

The lift coefficient for the experiment does show a 0.037 reduction by turning off the bottom two slots as presented in Table 5. This table also shows that the CFD for the two models were able to predict the corrected C_L within the measurement accuracy. Whereas, the SST model only shows a small download reduction for the U-configuration compared to the Ux45-configuration, the SA model shows an additional reduction of the download of 0.048.

Flow Control Performance A summary of the fuselage forces for all the configurations is given in Tables 6 and 7 with the percentage of drag and download reduction based on the respective baseline cases. The AFC U-configuration shows an experimental drag reduction of 26% with an uncertainty of $\pm$1% due to the uncertainty in the drag coefficient. The SST model results predict a drag reduction of 19%, which is much lower than the experimental value of 26% and falls outside the experimental uncertainty range. The SA model greatly over predicts the drag reduction at 43% and is more than twice the experimental drag reduction.

The experimental drag reduction performance for the Ux45-configuration is 27% and is similar to the U-configuration considering the $\pm$1% uncertainty in the data. The SST model under predicts the drag performance for this case at 13% with the SA model over predicting the flow control performance at 32%.

AFC Fuselage Drag Summary
Jet VR = 2.6, Ux45-configuration,100 knots, $AoA = -6^\circ$, $\mu = 0.25$, and $C_T/\sigma = 0.075$

	Jet VR	$\dot{m}(lbm/s)$	C_μ	$C_{D,visc}$	$C_{D,press}$	$C_{D,thrust}$	$C_{D,total}$	
CFD SA	2.6	0.127	0.016	0.044	0.106	-0.015	0.134	
CFD SST	2.6	0.127	0.016	0.041	0.118	-0.015	0.143	
EXP	2.6	0.127	0.016				0.185	$\pm$ 0.009
EXP CORRECTED	2.6	0.127	0.016				0.165	$\pm$ 0.009

Table 4. Summary of fuselage drag coefficient for AFC steady blowing for the Ux45-configuration.

AFC Fuselage Lift Summary
Jet VR = 2.6, Ux45-configuration, 100 knots, $AoA = -6^\circ$, $\mu = 0.25$, and $C_T/\sigma = 0.075$

	Jet VR	$\dot{m}(lbm/s)$	C_μ	$C_{L,visc}$	$C_{L,press}$	$C_{L,thrust}$	$C_{L,total}$	
CFD SA	2.6	0.127	0.016	0.003	-0.125	0.004	-0.124	
CFD SST	2.6	0.127	0.016	-0.003	-0.135	0.004	-0.134	
EXP	2.6	0.127	0.016				-0.133	$\pm$ 0.03
EXP CORRRECTED	2.6	0.127	0.016				-0.141	$\pm$ 0.03

Table 5. Summary of fuselage lift coefficient for AFC steady blowing for the Ux45-configuration.

Fuselage Drag Summary
100 knots, $AoA = -6^\circ$, $\mu = 0.25$, and $C_T/\sigma = 0.075$

		Drag Coefficient, C_D			Percentage Change C_D		
	C_μ	Exp_{corr}	SST	SA	Exp_{corr} %	SST %	SA %
BASELINE	0.000	0.225 $\pm$ 0.009	0.165	0.198	-	-	-
AFC U	0.021	0.166 $\pm$ 0.009	0.134	0.112	26% $\pm$ 1%	19%	43%
AFC UX45	0.016	0.165 $\pm$ 0.009	0.143	0.134	27% $\pm$ 1%	13%	32%

Table 6. Summary of fuselage drag for the baseline and AFC cases.

Fuselage Lift Summary
100 knots, $AoA = -6^\circ$, $\mu = 0.25$, and $C_T/\sigma = 0.075$

		Lift Coefficient, C_L			Percentage Change C_L		
	C_μ	Exp_{corr}	SST	SA	Exp_{corr}%	SST %	SA %
BASELINE	0.000	-0.287 $\pm$ 0.03	-0.190	-0.325	-	-	-
AFC U	0.021	-0.178 $\pm$ 0.03	-0.139	-0.172	38% $\pm$ 5%	27%	47%
AFC UX45	0.016	-0.141 $\pm$ 0.03	-0.134	-0.124	51% $\pm$ 5%	29%	62%

Table 7. Summary of fuselage lift for the baseline and AFC cases.

The experimental download performance for the U-configuration is 38% with the uncertainty range of $\pm$5% due to the measurement resolution of the balance in the normal force direction. The SST model under predicts the download reduction at 27% with the SA model over predicting at 47% with both CFD predictions falling outside of the experimental uncertainty range.

The Ux45-configuration shows an increased experimental download reduction of 51% by turning off the bottom two slots. This reduces the upflow on the ramp reducing the download force on the fuselage. The SST model under predicts the download for the Ux45-configuration at 29% and is not within the $\pm$5% experimental uncertainty. The SA model over predicts the download at 62% and is outside the uncertainty range of the experiment but is closer to the experimental download performance than the SST model.

Overall, both RANS turbulence models have a difficult time predicting the measured fuselage forces as well as the performance of the flow control for both the U and Ux45-configurations. The experimental uncertainty for the download is fairly high but the CFD results still fall outside of this range.

Centerline Pressures

In this section we compare the mean centerline C_p profiles between the CFD and wind tunnel data with and without flow control. The CFD C_p profiles are averaged over one rotor revolution after the transient forces on the fuselage have dissipated and the flow has reached a near periodic state. Figures 9 and 10 show the instantaneous C_p profiles for the baseline configuration using the SA model simulation over the last

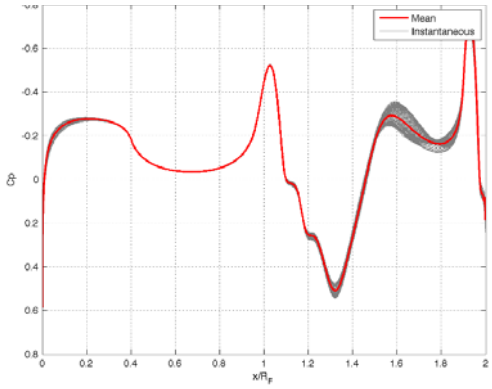

Fig. 9. CFD mean and instantaneous centerline lower Cp profiles for the baseline (no flow control) case using the SA turbulence model, AoA $= -6^{\circ}$, $\mu = 0.25$, and $C_T/\sigma = 0.075$.

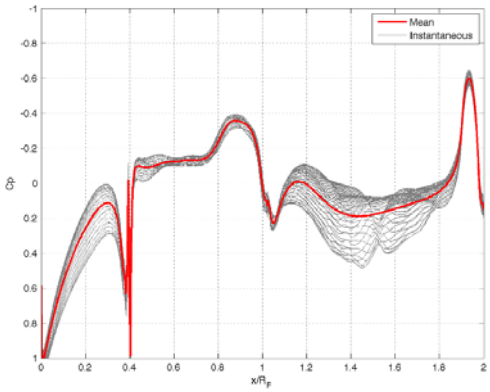

Fig. 10. CFD mean and instantaneous centerline upper Cp profiles for the baseline (no flow control) case using the SA turbulence model, AoA $= -6^{\circ}$, $\mu = 0.25$, and $C_T/\sigma = 0.075$.

rotor revolution. The instantaneous C_p profiles are sampled every 4.5° of rotor azimuth resulting in a total of 80 samples per revolution. Figure 9 shows the lower centerline C_p profiles with little variation and the largest unsteadiness seen on the tail. The upper centerline C_p profiles in Fig. 10 have large oscillations in pressure on the nose and tail sections as a result of the rotor interference. These unsteady variations in the fuselage surface pressures result in the large oscillations in the fuselage lift and drag forces shown in Fig. 8.

Baseline Case The lower centerline C_p profiles for the baseline case in Fig. 11 show a slight under prediction of the suction pressure on the lower nose section from x/R_F of 0.1 to 0.35 for both the SA and SST turbulence models. From a CFD point of view, this is a region where the simulation results are expected to match the experiment well and is a good indicator if the CFD has correctly modeled the flow conditions, model geometry, and fuselage AoA. At this point in time, the source for the small difference in C_p values ($\Delta C_p = 0.025$) on the nose section is not known.

The baseline CFD results in Fig. 11 also do not match the lower centerline pressure gradient measured between x/R_F of 0.5 and 0.7. The C_p values at x/R_F of 0.5 and 0.6 show a small difference whereas the C_p value at x/R_F of 0.7 is much lower for the experiment compared to the CFD. This is true for all the CFD cases in this paper. The source of these differences is not known at this time.

For this investigation, accurate modeling of the pressure on the ramp is critical in order to predict the fuselage drag. Comparisons of the centerline C_p profiles on the ramp are therefore a strong indicator on how well the CFD is able to model the flow on the ramp, and thus predict fuselage drag. One of the key features in the centerline pressure profile is the suction peak on the lower portion of the ramp. This suction peak is very sensitive to the flow separation on the curved surface at the edge of the lower ramp and is an ideal location to compare to the CFD results. Unfortunately, pressure measurements capturing this suction peak were not possible due to the placement of additional flow control actuators. However, comparisons of the baseline lower centerline C_p profile on the ramp in Fig. 11 show that the SA model predicts a significantly larger suction peak at x/R_F of 1.02 than the SST model. Further investigation revealed that the SA model predicts the flow to remain attached longer on the lower ramp centerline than the SST model, resulting in a larger suction peak. The comparison shows the SA model matches the experimental C_p values on the upper portion of the ramp, while over predicting the pressure on the lower portion of the ramp from x/R_F of 1.12 to 1.18. The SST model results show an under prediction of the pressure on the upper portion of the ramp with a similar over prediction on the lower portion of the ramp.

The fuselage drag in Table 6 does show the SST model having a lower drag than the SA model. This is inconsistent with the ramp centerline pressure being higher for the SA model as compared to the SST. One explanation may be that the suction pressure on the bottom and sides of the fuselage is much higher when the flow is attached, as is the case for the SA model simulation. If this suction pressure is large it can negate any reduction in the drag due to the increased pressure on the center of the ramp. Therefore, the resulting net drag becomes a balance between the increased pressure on the center of the ramp and the low pressure on the sides and bottom.

The C_p values on the upper surface centerline of the fuselage nose section in Fig. 12 compare well to the experimental data for both CFD turbulence models. This is also a region where it is expected that the CFD will match the experiment and is a good check on how well the CFD is modeling the correct flow conditions, fuselage AoA, and rotor downwash. The C_p values at x/R_F of 0.45 and 0.90 do not match the experimental data very well. These pressures are affected by the presence of the rotor hub that is not modeled in the CFD sim-

ulations for this paper. Therefore, it is expected that the CFD will not match the pressure at these locations.

AFC Steady Blowing Case: U-Configuration A comparison of the centerline C_p profiles for the AFC U-configuration are given in Figs. 13 and 14. This steady blowing case has an improved CFD prediction of the C_p centerline profile on the lower nose and ramp regions as compared to the baseline case. As was seen in the baseline case, the SA model has a larger suction pressure peak at $x/R_F = 1.02$ than the SST model as a result of the early flow separation predicted by the SST model. The ramp pressures are predicted very well using the SST model with the SA model over predicting the centerline C_p values. This higher ramp pressure predicted by the SA model is consistent with the under prediction of the fuselage drag presented in Table 6.

As was seen in the baseline case, the upper centerline C_p values in Fig. 14 compare well to the experiment, providing confidence that the CFD is correctly modeling the fuselage AoA and rotor effects. As discussed in the baseline case, the pressures on the upper pylon do not match the experiment well since the rotor hub is not being modeled.

AFC Steady Blowing Case: Ux45-Configuration A comparison of the centerline C_p profiles for the AFC Ux45-configuration are given in Figs. 15 and 16. As with the previous U-configuration, the lower centerline nose pressures are predicted very well. The Ux45-configuration shows a decrease in the suction peaks at the bottom of the ramp for both the SA and SST turbulence models. This indicates that the flow on the bottom of the ramp has separated farther upstream than the AFC U-configuration. This is expected since the bottom two AFC slots (4 & 5) are turned off and don't provide control to attach the flow on this portion of the ramp. The experiment shows a fairly flat pressure region as on the bottom of the ramp centerline where the SA and SST models over predict these pressures. While the SST model shows better agreement with the experiment than the SA model, there are considerable differences between SST results and the experimental data on the ramp.

Ramp Span Pressures

In this section we compare the mean spanwise surface pressures on the ramp with and without flow control. Figure 17 shows a rear view of the ramp and the location of the spanwise pressure measurements. The spanwise C_p profiles on the ramp were averaged over the last rotor revolution in the same way the centerline C_p profiles were averaged.

Baseline Case Figure 18 compares the baseline CFD spanwise C_p profiles to the measured values from the experiment. This plot is a top view of the model, such that positive y/R_F values are on the advancing blade side and negative values are on the retreating side. This figure shows that the experiment does not resolve the suction peaks on the sides of the fuselage due to the limited number of orifices and their spacing. Unfortunately, the actuators inside the model prevented additional pressure measurements needed to capture the side suction pressure peaks. The measurements do capture the suction rise approaching the sides of the ramp but there is not enough resolution to positively identify the suction peak for this case. Comparing the SA model C_p profile to the measured data suggests that the experimental suction peaks may be near the pressure ports at $y/R_F = \pm 0.157$. The SA model results accurately predict a larger suction pressure on the advancing rotor side of the fuselage as seen in the experiment. The SST model, however, has a much lower suction peak indicating that the flow on the sides of the fuselage separate farther upstream than the SA model and the experiment. This is consistent with the lower centerline comparisons where the SST model had a much lower suction peak and may explain why the predicted drag is lower when using the SST model compared to the drag predicted using the SA model. The SA model predicts a lower pressure (higher suction) near the edges of the ramp, which directly contributes to an increase in drag.

AFC Steady Blowing Case: U-Configuration Spanwise profiles of C_p for the AFC U-configuration are compared in Fig. 19. In this comparison, both turbulence models fail to match the pressure on the sides of the fuselage as well as the pressure in the middle of the ramp. Thus, indicating that the CFD is not correctly resolving the flow separation on the sides of the fuselage for this blowing configuration. The experiment was able to capture the suction peak on the retreating blade side of the fuselage ($y/R_F = -0.16$) but not on the advancing side. The SA model results show a much higher C_p value in the middle of the ramp span, which is consistent with the over prediction of the drag reduction given in Table 6.

AFC Steady Blowing Case: Ux45-Configuration The results for the AFC Ux45-configuration are compared in Fig. 20. This comparison shows that the CFD was not able to accurately predict the spanwise pressures on the ramp. The SA model results do match the suction peak on the rotor advancing side of the fuselage but over predict the suction peak on the rotor retreating side. Both models over predict the back pressure in the middle of the ramp span.

Ramp Surface Pressures

Figures 21 to 23 show a rear view of the ramp for the CFD simulations using the SA and SST turbulence models for the baseline and two AFC cases. The fuselage surface is shaded by the instantaneous C_p values with surface restricted streamlines and the slot locations outlined in red. These figures were made for a blade azimuthal angle of 0° after the fuselage forces have reach a near periodic state.

Baseline Case The baseline CFD results using the SA model in Fig 21 show flow separation near the slot locations with the exception of the upper right portion of the ramp. However, the

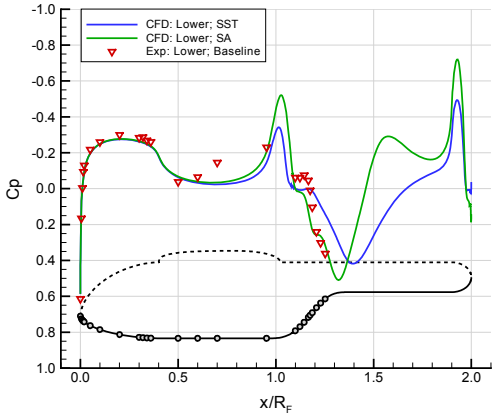

Fig. 11. Centerline lower Cp profile comparison between CFD and experiment for the baseline (no flow control) case, AoA $= -6^{\circ}$, $\mu = 0.25$, and $C_T/\sigma = 0.075$.

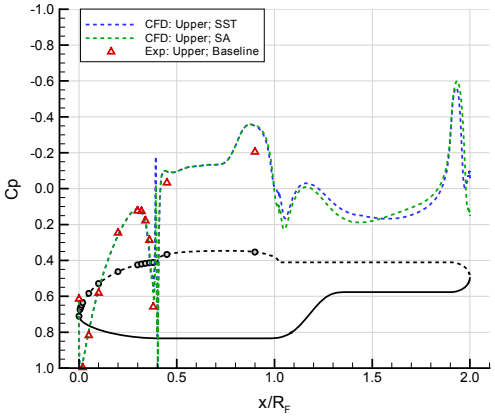

Fig. 12. Centerline upper Cp profile comparison between CFD and experiment for the baseline (no flow control) case, AoA $= -6^{\circ}$, $\mu = 0.25$, and $C_T/\sigma = 0.075$.

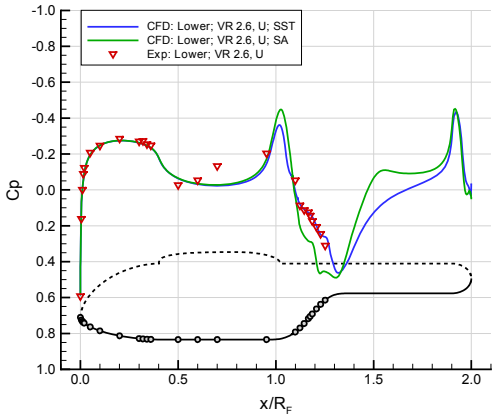

Fig. 13. Centerline Cp lower profile comparison between CFD and experiment for the flow control case with a jet velocity ratio of 2.6 for the full U-configuration, AoA $= -6^{\circ}$, $\mu = 0.25$, and $C_T/\sigma = 0.075$.

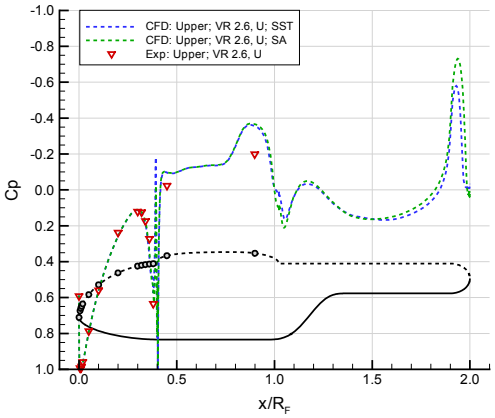

Fig. 14. Centerline Cp upper profile comparison between CFD and experiment for the flow control case with a jet velocity ratio of 2.6 for the full U-configuration, AoA $= -6^{\circ}$, $\mu = 0.25$, and $C_T/\sigma = 0.075$.

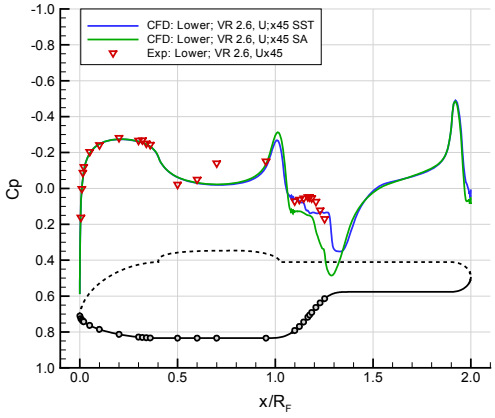

Fig. 15. Centerline Cp lower profile comparison between CFD and experiment for the flow control case with a jet velocity ratio of 2.6 for the Ux45-configuration, AoA $= -6^{\circ}$, $\mu = 0.25$, and $C_T/\sigma = 0.075$.

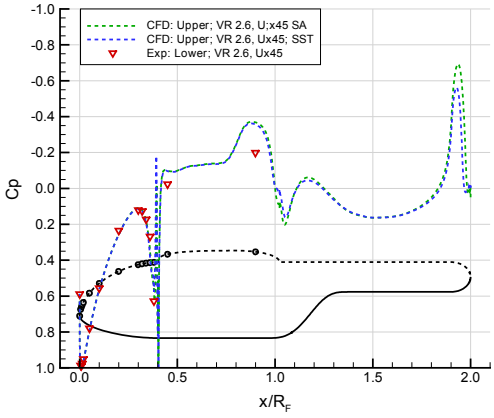

Fig. 16. Centerline Cp upper profile comparison between CFD and experiment for the flow control case with a jet velocity ratio of 2.6 for the Ux45-configuration, AoA $= -6^{\circ}$, $\mu = 0.25$, and $C_T/\sigma = 0.075$.

CFD predictions using the SST model predict flow separation farther upstream for the lower portion of the ramp with a different flow separation pattern on the upper portion. The SA model predicts more attached flow on the ramp than the SST model with higher C_p values in the middle of the ramp. The SA model also shows a low pressure region on the sides of the ramp as a result of the attached flow accelerating around the curved surface.

AFC Steady Blowing Case: U-Configuration The effects of the flow control on the ramp pressure are shown in Fig. 22 for the U-configuration. A comparison between the baseline and the AFC U-configuration show a significant increase in the ramp surface pressure. This increase in the ramp pressure directly results in a reduction of the pressure drag on the fuselage. The SA model results show a much stronger effect of the blowing on the ramp pressure than the SST model. As was seen in the drag predictions, the SA model resulted in larger drag reduction compared to the SST model with both models under predicting the experimental drag. The SST model does have a larger extent of flow separation on the lower right portion of the ramp compared to the SA model. This larger separation region predicted by the SST model would explain why the ramp pressures are lower compared to the ramp pressures predicted using the SA model.

AFC Steady Blowing Case: Ux45-Configuration Figure 23 shows the ramp surface pressure and streamlines for the Ux45-configuration where turning off the bottom two slots resulted in the flow separating farther upstream on the bottom of the ramp. The C_p contours also show lower pressure on the ramp compared to the U-configuration. While the experiment did not show an increase in drag from the U-configuration to Ux45-configurations, the CFD predictions do show an overall drag increase. This drag increase may be attributed to the decrease in the pressure on the ramp from the U to Ux45-configuration seen in Figs. 22 and 23.

PIV Data

Figures 24 to 26 compare the measured flow field downstream of the fuselage ramp to the CFD results for the baseline and AFC cases. Contour plots of the streamwise velocity, U, spanwise velocity, V, and vertical velocity, W, are shown with a black rectangle outlining the location of the PIV field of view.

Baseline Case For the baseline case shown in Fig. 24, the SA model compares well to the PIV data for the three components of velocity. The SST model shows a large deficit in the streamwise velocity that is consistent with the prediction of a larger flow separated region on the ramp. The vertical velocity contours show that the SA model results match well with the PIV data, however, the SST model under predicts the upflow velocity under the tail boom. The under prediction of the upflow velocity by the SST model is a result of the early flow separation on the lower portion of the ramp. The magnitude of the upflow is also related to the fuselage download force as discovered by Martin et al. (Ref. 8). The larger the upflow velocity the larger the download force on the fuselage. The reduced upflow velocity by the SST model is consistent with the download force results shown in Table 7.

AFC Steady Blowing Case: U-Configuration Fuselage wake data for the AFC U-configuration case is compared in Fig. 25. The streamwise velocity contours show good agreement between the SA model and the PIV data with the SST model showing a larger wake deficit. The spanwise velocity does not show the same trend with the SST model comparing fairly well to the PIV data and the SA model showing lower spanwise velocities than the experiment. Both the SA and SST models under predict the upflow velocity with the SST model showing better agreement to the experiment than the SA model. This is reflected in the download forces given in Table 7 where the SA and SST model results under predict the experimental download force.

AFC Steady Blowing Case: Ux45-Configuration The fuselage wake comparison data for the AFC Ux45-configuration is shown in Fig. 26. This case shows that turning off the bottom two slots results in a large wake deficit compared to the U-configuration. Both the SA and SST models compare well to the PIV data with the SST model showing a slightly larger wake. The biggest difference from the baseline to the AFC U-configuration is the significant reduction in the upflow velocity, correlating to the reduction of the fuselage download force. The CFD simulations capture the additional reduction in vertical velocity in the wake for the Ux45-configuration.

Iso-Surface Contours

Iso-surface contours of vorticity magnitude are shown in Fig. 27 from the CFD simulations using the SA turbulence model. These iso-surface contours are for a single vorticity magnitude value and are shaded by the local pressure coefficient. These plots are informative, showing the interaction of the rotor wake on the tail section and the wake from the ramp region. The rotor wake is shown to pass over the upper part of the ramp and tail section. From these iso-surface contours it can be seen that the rotor wake for this advance ratio does not directly interact with the ramp. The baseline case also shows the wake from the ramp moving upward towards the tail where the two AFC cases show the wake moving in the streamwise direction.

SUMMARY

Wind tunnel experiments conducted at the 14-by 22-Foot Subsonic Tunnel at NASA Langley Research Center have demonstrated the ability of flow control to reduce rotorcraft fuselage drag and download forces in the presence of a rotor in forward flight. A key element to the wind tunnel test was to provide measurements that would support CFD validation. Specifically, the ability of CFD to predict the performance of flow

control for fuselage drag and download reduction. Towards this CFD validation effort, the flow solver code, OVERFLOW, developed at NASA, was used to provide an assessment of the CFD and wind tunnel data for validation. The CFD approach in this study solved the unsteady Reynolds-averaged Navier-Stokes (RANS) equations using the SA and SST turbulence models.

1. The drag and lift coefficients for the fuselage were compared between the experiment and CFD simulations. The comparison showed that the CFD simulations did predict a drag and download reduction on the fuselage with flow control but were unable to match the measured drag and lift coefficients. The CFD was also unable to predict the performance of the flow control in terms of a percentage of drag or download reduction for a given value of C_μ or actuator configuration.

2. A comparison of the fuselage centerline surface pressures showed that the CFD was able to predict the pressures on the nose of the fuselage but had difficulty fully predicting the centerline pressures on the ramp. The SA model was able to predict the baseline centerline pressures on the ramp well but did not fully match the experiment on the lower portion of the ramp. The SST model did not match the ramp centerline pressure for the baseline due to early flow separation on the ramp.

3. The steady blowing case for the U-configuration (all eight slots) showed the SST model to have a very good prediction of the centerline pressures on the ramp with the SA model over predicting the ramp centerline pressures. The Ux45-configuration (bottom two slots off) proved difficult for both models to fully predict. For this configuration the SST model showed a better prediction over the SA model.

4. A row of pressure measurements across the ramp in the spanwise direction provided a measure of the back pressure on the ramp as well as the suction pressure on the ramp sides. For the baseline case, the SA model was found to match the suction pressure measured on the sides of the ramp but not the C_p values in the middle of the ramp. The SST model under predicted the suction pressure on the sides, indicating that the SST model results separated farther upstream compared to the SA model and the experiment. For the flow control cases, both the SA and SST models were not able to match the measured C_p spanwise profiles on the ramp, missing the suction pressure on the sides and the back pressure on the middle of the span.

5. Off body flow measurements using Stereo PIV provided valuable flow field data of the fuselage wake for CFD validation. The baseline case showed that the SA model did well modeling the wake of the fuselage but did not fully match the measured flow field data. The SST model baseline results had a very large wake deficit not seen in the PIV measurements. This indicated that the large flow separation predicted by the SST model for the baseline flow was not consistent with the experiment. The flow control cases did show that the SA and SST models were able to capture the correct flow features but did not consistently match the velocity levels.

In summary, the RANS CFD simulations using the SA and SST models were unable to predict the flow control performance for the fuselage drag and download forces. The CFD had some success in predicting fuselage pressures but had trouble fully predicting the pressures on the ramp. The CFD did fairly well predicting the wake features from the fuselage but tended to be inconsistent in matching the velocity levels measured in the experiment.

It is recommended that future CFD simulations consider using turbulence models, such as Detached Eddy Simulation (DES) that are more capable of modeling bluff body flows such as the flow on the fuselage ramp.

ACKNOWLEDGMENTS

This work was supported by the NASA Rotary Wing Project and the support of Susan A. Gorton, Project Manager, is gratefully acknowledged. This work would not have been possible without the hard work and dedication of the Army/NASA rotorcraft team at NASA Langley and the entire 14x22 staff. All of the computations in this paper were performed on the NASA Advanced Supercomputing (NAS) machines. Special thanks to all of the NAS staff for their ongoing support of the NAS machines.

REFERENCES

[1]Leishman, J. G., *Principles of Helicopter Aerodynamics*, Cambridge University Press, second edition, 2006.

[2]Gatard, J., Costes, M., Kroll, N., Renzoni, P., Kokkalis, A., Rocchetto, A., Serr, C., Larrey, E., Filippone, A., and Wehr, D., "High Reynolds Number Helicopter Fuselage Test in the ONERA F1 Pressureized Wind Tunnel," 23rd European Rotorcraft Forum Paper 167, Dresden, Germany, September 16-18, 1997.

[3]Martin, P., Tung, C., Hassan, A., Cerchie, D., and Roth, J., "Active Flow Control Measurements and CFD on a Transport Helicopter Fuselage," American Helicopter Society 61^{st} Annual Forum, Grapevine, TX, 2005.

[4]Ben-Hamou, E., Arad, E., and Seifert, A., "Generic Transport Aft-Body Drag Reduction using Active Flow Control," AIAA Paper 2004-2509, 2004.

[5]Schaeffler, N. W., Allan, B. G., Lienard, C., and Le Pape, A., "Progress Towards Fuselage Drag Reduction via Active Flow Control: A Combined CFD and Experimental Effort," The 36^{th} European Rotorcraft Forum, Paris, France, September 2010.

[6]Freeman, C. and Mineck, R. E., "Fuselage Surface Pressure Measurments of a Helicopter Wind-Tunnel Model with a 3.15-meter Diameter Single Rotor," NASA TM 80051, Langley Research Center, March 1979.

[7]Allan, B. G. and Schaeffler, N. W., "Numerical Investigation of Rotorcraft Fuselage Drag Reduction using Active Flow Control," The American Helicopter Society 67^{th} Annual Forum, Virginia, VA, May 2011.

[8]Martin, P. B., Overmeyer, A. D., Tanner, P. E., Wilson, J. S., and Jenkins, L. N., "Helicopter Fuselage Active Flow Control in the Presence of a Rotor," The American Helicopter Society 70^{th} Annual Forum, Montréal, Québec, Canada, May 2014.

[9]Schaeffler, N. W., Allan, B. G., Wong, O. D., and Tanner, P. E., "Experimental Investigation of Active Aerodynamic Load Reduction on a Rotorcraft Fuselage with Rotor Effects," AIAA Paper 2014-2561, June 2014.

[10]Lienard, C., Le Pape, A., and Verbeke, C., "Numerical and Experimental Investigation of Helicopter Fuselage Drag Reduction Using Active Flow Control," The American Helicopter Society 68^{th} Annual Forum, Fort Worth, TX, May 2012.

[11]Lienard, C., Le Pape, A., Verbeke, C., Pruvost, M., and Coninek, J.-L. D., "Helicopter Fuselage Drag Reduction Using Active Flow Control: a Comprehensive Experimental Investigation," The American Helicopter Society 69^{th} Annual Forum, Phoenix, AZ, May 2013.

[12]Buning, P. G., Jespersen, D. C., Pulliam, T. H., Klopfer, W. M., Chan, W. M., Slotnick, J. P., Krist, S. E., and Renze, K. J., "OVERFLOW User's Manual Version 1.8m," NASA Langley Research Center, 1999.

[13]Jespersen, D., Pulliam, T., and Buning, P., "Recent Enhancements to OVERFLOW," AIAA Paper 97–0644, January 1997.

[14]Pulliam, T. H. and Chaussee, D. S., "A Diagonal Form of an Implicit Approximate-Factorization Algorithm," *Journal of Computational Physics*, Vol. 39, February 1981, pp. 347–363.

[15]Steger, J. L., Dougherty, F. C., and Benek, J. A., "A Chimera Grid Scheme," Advances in Grid Generation, edited by K. N. Ghia and U. Ghia, Vol. 5, FED, 1983.

[16]Spalart, P. and Allmaras, S. R., "One-Equation Turbulence Model for Aerodynamic Flows," AIAA Paper 1992-0439, 1992.

[17]Menter, R. F., "Two-Equation Eddy-Viscosity Turbulence Models for Engineering Applications," *AIAA Journal*, Vol. 32, (8), 1994, pp. 1598–1605.

[18]Shur, M., Strelets, M., Travin, A., and Spalart, P., "Turbulence Modeling in Rotating and Curved Channels: Assessing the Spalart-Shur Correction," *AIAA Journal*, Vol. 38, (5), May 2000, pp. 784–792.

[19]Johnson, W., "Rotorcraft Aerodynamics Models for a Comprehensive Analysis," American Helicopter Society 54th Annual Forum Proceedings, Washington, D.C., May 20-22, 1998.

[20]Johnson, W., "CAMRAD II Comprehensive Analytical Model of Rotorcraft Aerodynamics and Dynamics," Johnson Aeronautics, Palo Alto, Californinia, 2005.

[21]Murrill, R., "Operation and Maintenance Manual for the General Rotor Model System," NASA CR-145230, May 1977.

[22]Wong, O. D., Noonan, K. W., Watkins, A. N., Jenkins, L. N., and Yao, C. S., "Non-Intrusive Measurements of a Four-Bladed Rotor in Hover A First Look," The American Helicopter Society Fifth Decennial AHS Aeromechanics Specialists' Conference, San Francisco, CA, January 2010.

[23]Jenkins, L. N., Yao, C. S., Bartram, S., Harris, J., Allan, B., Wong, O., and Mace, D., "Development of a Large Field-of-View PIV System for Rotorcraft Testing in the 14x22 Subsonic Wind Tunnel," The American Helicopter Society 65^{th} Annual Forum, Ft. Worth, May 2009.

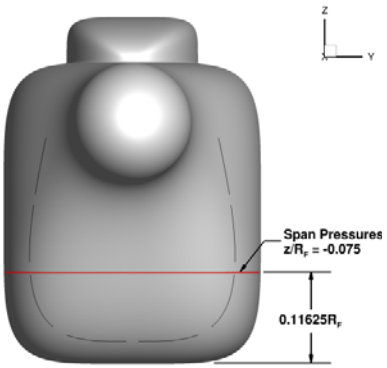

Fig. 17. Rear view of the ramp showing the location of the spanwise measurements at the $z/R_F = -0.075$.

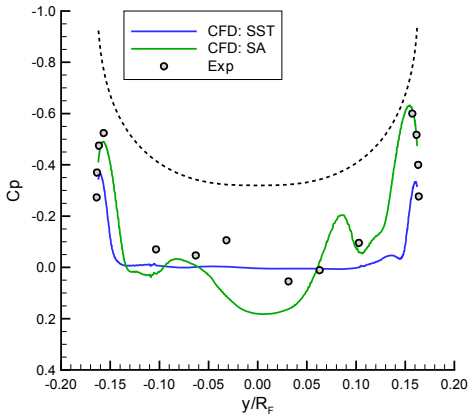

Fig. 18. Spanwise Cp profile comparison between CFD and experiment on the ramp for the baseline (no flow control) case, AoA $= -6^\circ$, $\mu = 0.25$, and $C_T/\sigma = 0.075$.

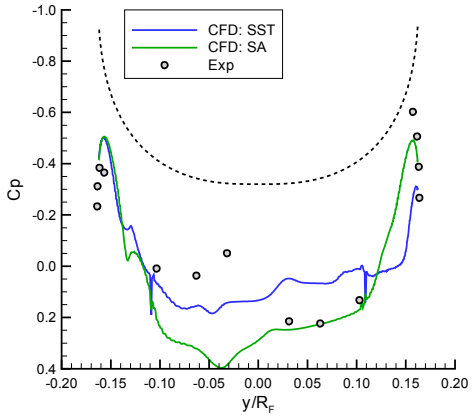

Fig. 19. Spanwise Cp profile comparison between CFD and experiment on the ramp for the flow control case with a jet velocity ratio of 2.6 for the U-configuration, AoA $= -6^\circ$, $\mu = 0.25$, and $C_T/\sigma = 0.075$.

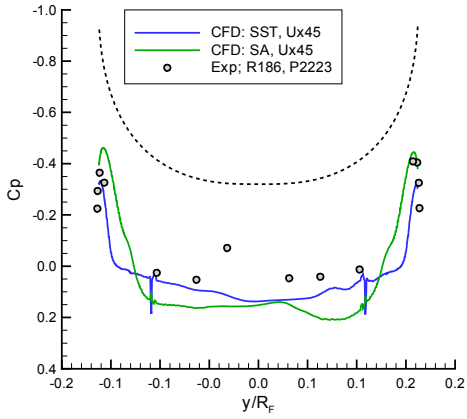

Fig. 20. Spanwise Cp profile comparison between CFD and experiment on the ramp for the flow control case with a jet velocity ratio of 2.6 for the Ux45-configuration, AoA $= -6^\circ$, $\mu = 0.25$, and $C_T/\sigma = 0.075$.

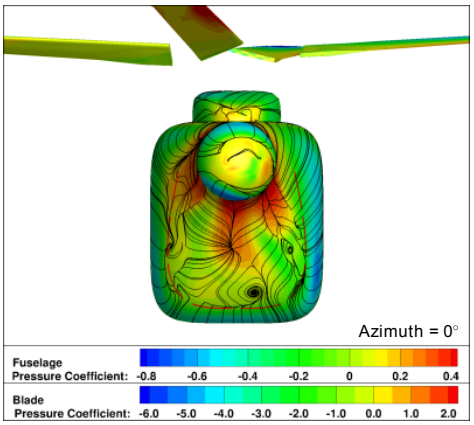

SA Baseline

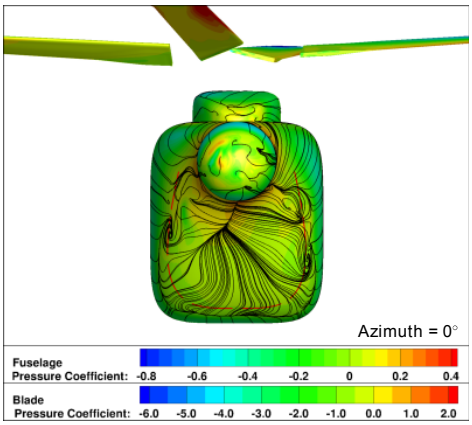

SST Baseline

Fig. 21. Baseline (no flow control) case showing a rear view of the ramp section with Cp contours and instantaneous surface restricted streamlines, AoA $= -6^{\circ}$, $\mu = 0.25$, and $C_T/\sigma = 0.075$.

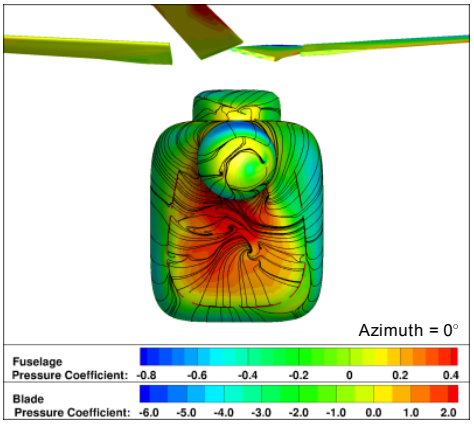

SA AFC, U

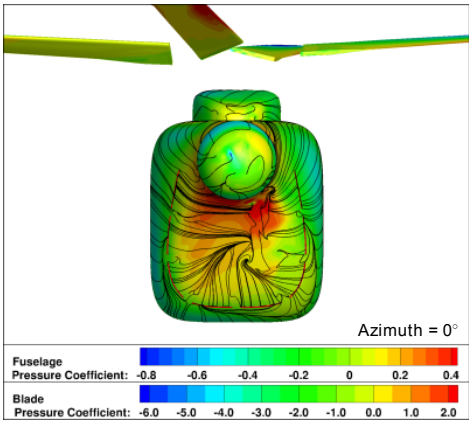

SST AFC, U

Fig. 22. Flow control case (jet velocity ratio of 2.6) for the U-configuration case showing a rear view of the ramp section with Cp contours and instantaneous surface restricted streamlines, AoA $= -6^{\circ}$, $\mu = 0.25$, and $C_T/\sigma = 0.075$.

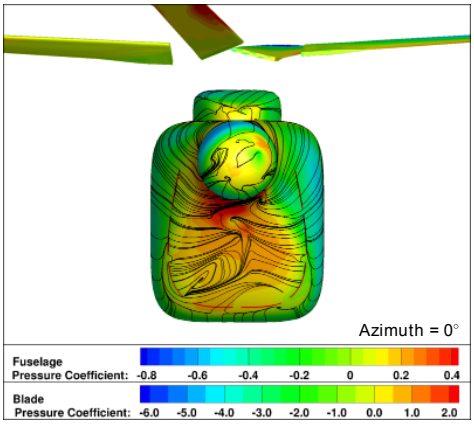

SA AFC, Ux45

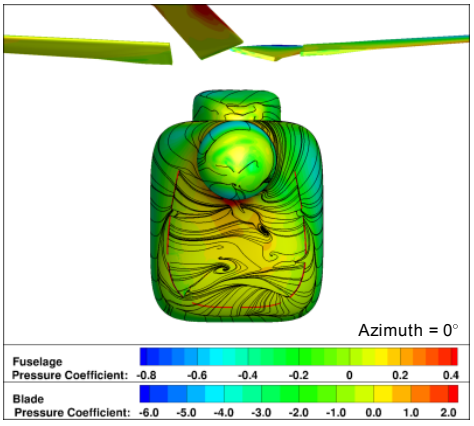

SST AFC, Ux45

Fig. 23. Flow control case (jet velocity ratio of 2.6) for the Ux45-configuration case showing a rear view of the ramp section with Cp contours and instantaneous surface restricted streamlines, AoA $= -6^{\circ}$, $\mu = 0.25$, and $C_T/\sigma = 0.075$.

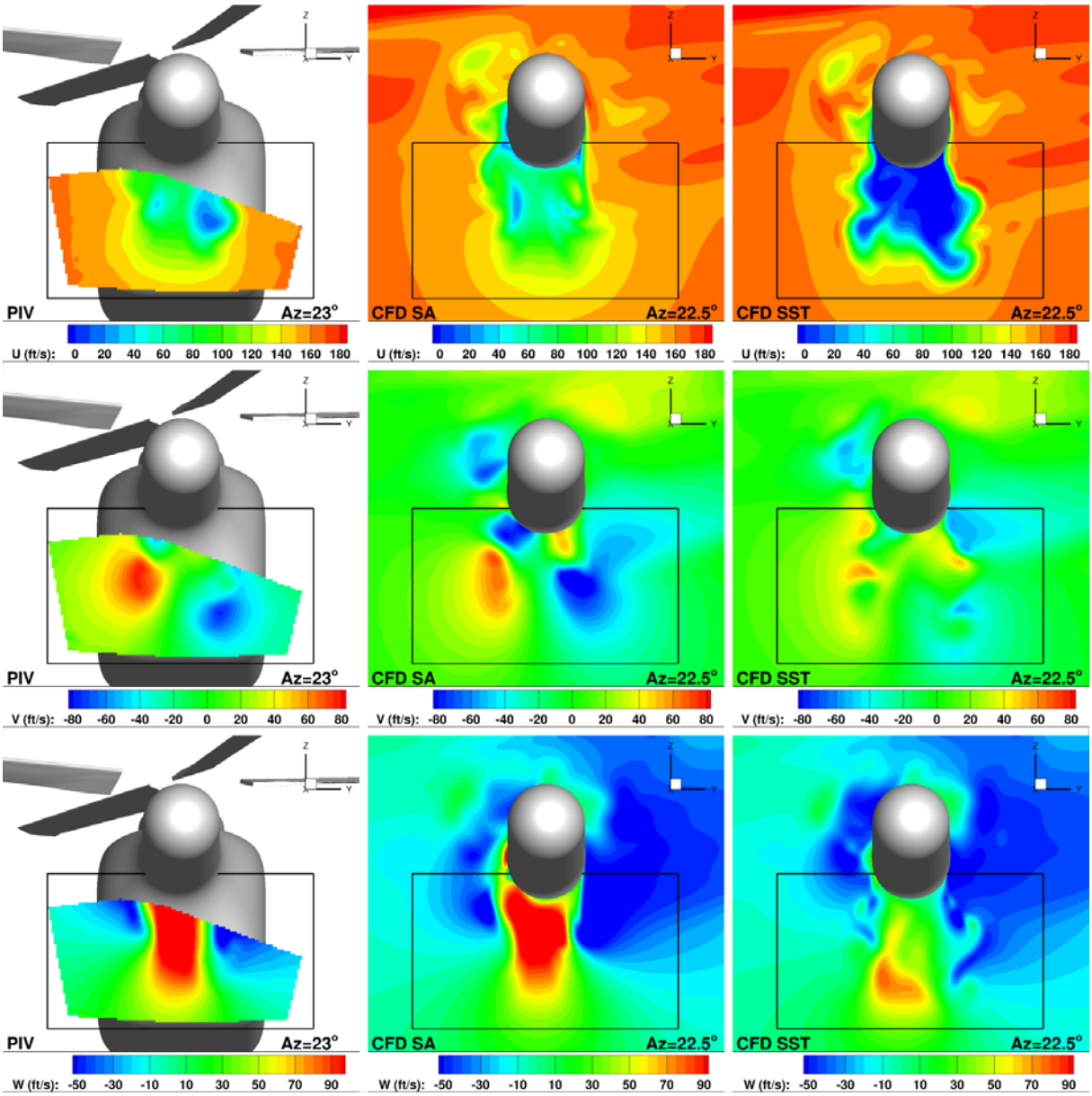

Fig. 24. Comparison of CFD and PIV data for the baseline. AoA $= -6^{\circ}$, $\mu = 0.25$, and $C_T/\sigma = 0.075$.

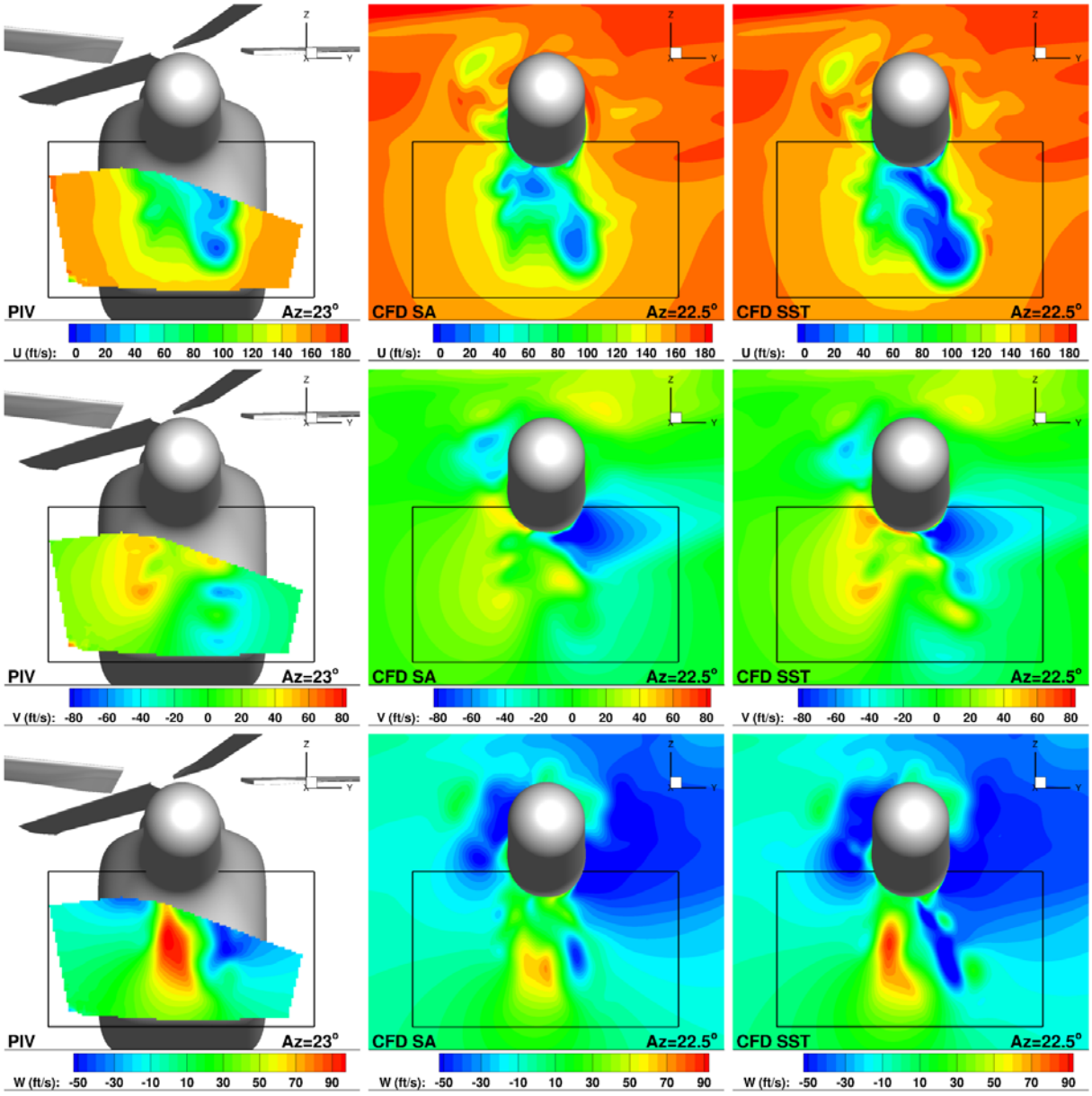

Fig. 25. Comparison of CFD and PIV data for the AFC jet VR=2.6 using full U-configuration. AoA $= -6^{\circ}$, $\mu = 0.25$, and $C_T/\sigma = 0.075$.

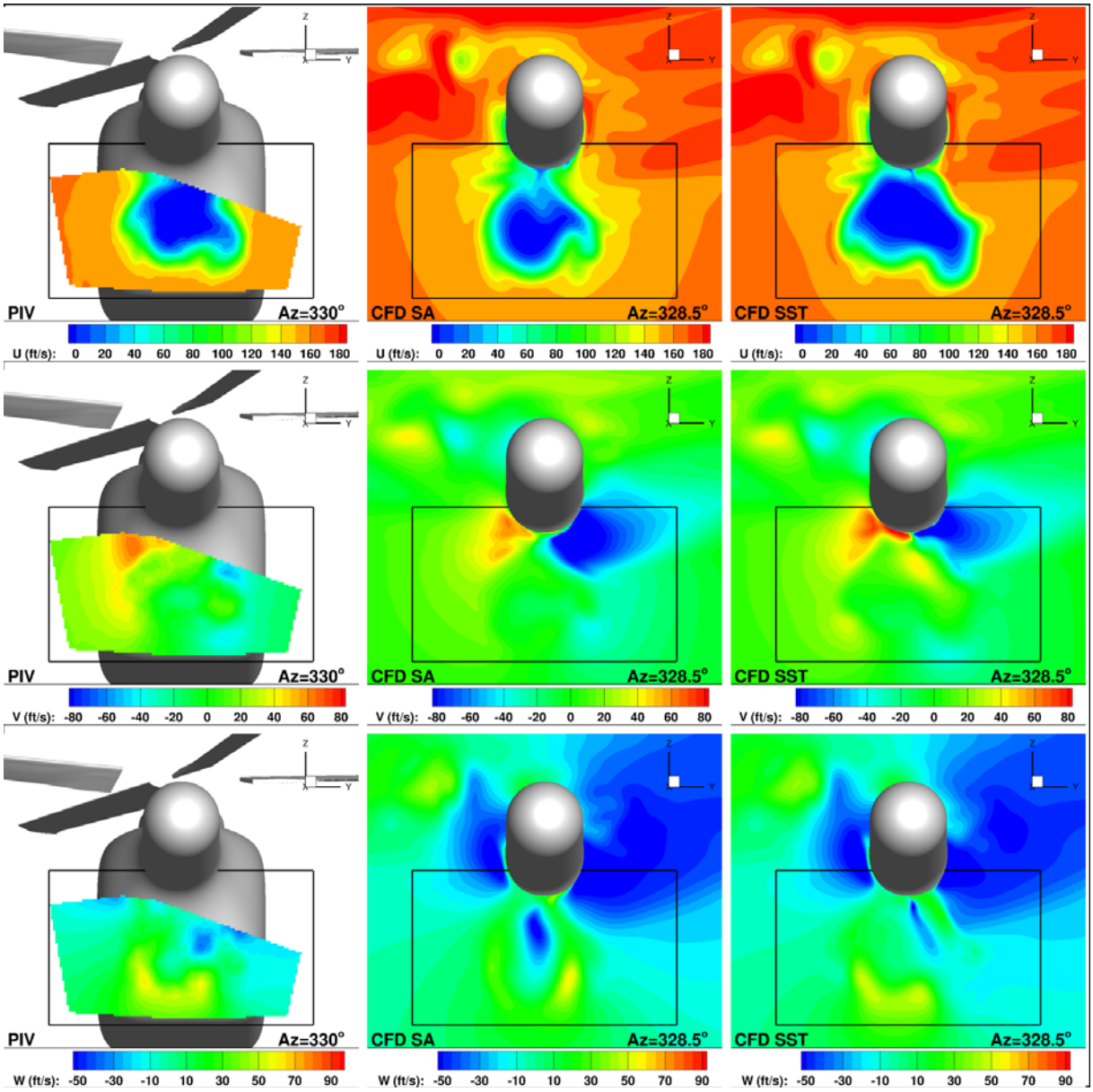

Fig. 26. Comparison of CFD and PIV data for the AFC jet VR=2.6 using Ux45-configuration. AoA $= -6^{\circ}$, $\mu = 0.25$, and $C_T/\sigma = 0.075$.

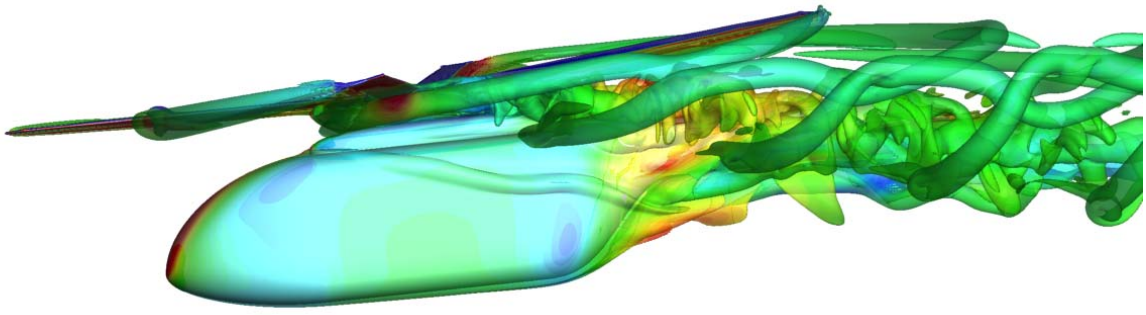

Baseline

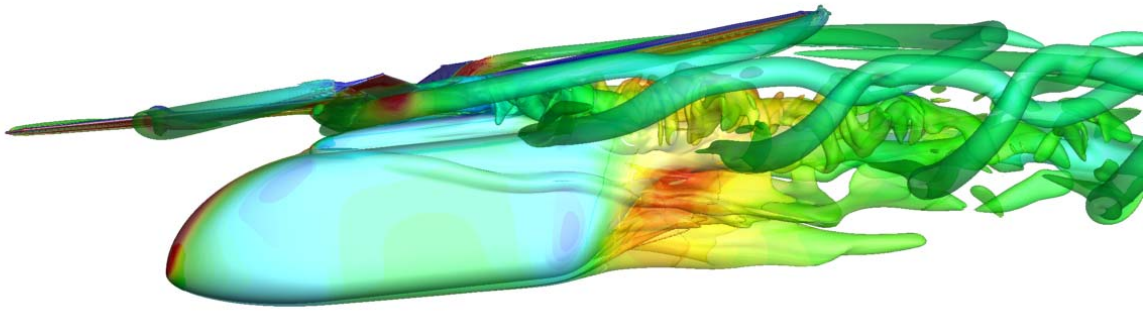

AFC, Jet VR 2.6, U-Configuration

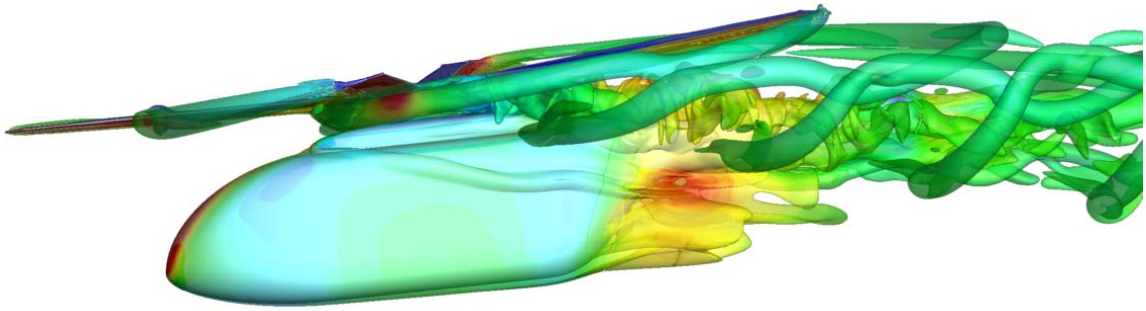

AFC, Jet VR 2.6, Ux45-Configuration

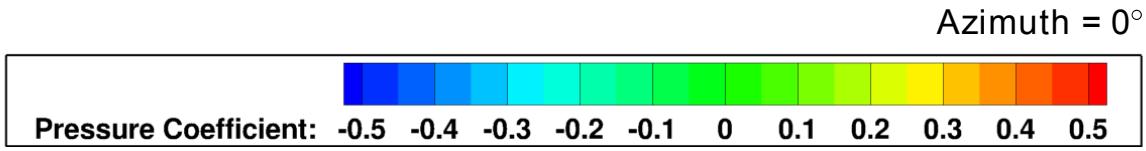

Fig. 27. Vorticity magnitude iso-surface contours shaded by Cp for the baseline, AFC U, and Ux45-configurations from the CFD simulations using the SA turbulence model, AoA $= -6^{\circ}$, $\mu = 0.25$, and $C_T/\sigma = 0.075$.